Computing Global Invariant Manifolds: Techniques and Applications

Hinke M. Osinga

Abstract. Global invariant manifolds play an important role in organising the behaviour of a dynamical system. Together with equilibria and periodic orbits, they form the so-called skeleton of the dynamics and offer geometric insight into how observed behaviour arises. In most cases, it is impossible to find invariant manifolds explicitly and numerical methods must be used to find accurate approximations. Developing such computational techniques is a challenge on its own and, to this date, the focus has primarily been on computing two-dimensional manifolds. Nevertheless, these computational efforts offer new insights that go far beyond a confirmation of the known theory. Furthermore, global invariant manifolds in dynamical systems theory not only explain asymptotic behaviour, but more recent developments show that they are equally useful for explaining short-term transient dynamics. This paper presents an overview of these more recent developments, in terms of novel computational methods, as well as applications that have stimulated recent advances in the field and highlighted the need for new mathematical theory.

Mathematics Subject Classification (2010). Primary 37C10; Secondary 37D10, 37C70, 65L10, 65P30.

Keywords. Dynamical systems, invariant manifold, boundary value problem, continuation techniques.

1. Introduction

Dynamical systems theory is very much characterised by its geometrical and topological aspects; classical textbooks, such as [6, 29, 33, 62, 63, 68], for example, rely on sketches to illustrate ideas. Therefore, it seems natural to have a computational toolbox that can produce numerical approximations to illustrate how this theory manifests itself in actual dynamical systems. The development of such a toolbox has proven to be a challenge in itself, which perhaps explains the apparent split of the field into those who use sketches and those who employ numerical computations; the two groups tend to interact too little. In fact, numerical computations are often used in realistic applications in collaboration with other scientists. There seems to exist a perception that this direction of research may lead to new numerical challenges, but does not contribute to the development of new theory, while theoreticians push the boundaries of dynamical systems and offer new insights via conjectures and then proofs. This paper aims to highlight how the development of

dedicated computational methods arising from real applications can also lead to new dynamical systems theory. The focus here will be on continuation methods for the computation of global invariant manifolds of vector fields.

Continuation methods for dynamical systems were designed for the bifurcation analysis of equilibria and periodic orbits. Pseudo-arclength continuation is used to track such invariant objects in a parameter [41]. Continuation of equilibria is relatively straightforward and involves finding an approximation to a uniquely defined parametrised solution family of an algebraic problem. The continuation of periodic orbits is already harder, because it requires solving a two-point boundary value problem (2PBVP) in conjunction with a suitable restriction to select a unique orbit from the infinite family of phase-shifted ones. The method of orthogonal collocation with piecewise polynomials [7, 10] is now widely adopted for this purpose, because it is very accurate and allows adaptive mesh selection; this particular solution method is implemented in the popular packages AUTO [16, 17], which is also part of the package XPPAUT [21], and MATCONT [15]. By extending the system to include suitable monitoring functions, the same approach can be used to continue codimension-one bifurcations in two parameters. In fact, the initiative behind the package MATCONT [15] aims to have implementations for the continuation of all codimension-one and -two bifurcations of equilibria and periodic orbits, both for continuous- and discrete-time deterministic systems [27, 46].

The continuation of periodic orbits is only one example of a 2PBVP set-up. Global invariant manifolds can also be formulated in terms of a 2PBVP. This idea has been applied to detect and continue homoclinic and heteroclinic bifurcations [36]. For example, the HOMCONT extension to AUTO can be used to compute such codimension-one bifurcations and determine the location of codimension-two points, such as homoclinic flip bifurcations [12]; these methods have also been developed for discrete-time systems [9], which is implemented for one-dimensional manifolds in the command-line version of MATCONT. Here, we apply the 2PBVP set-up in the context of computing two-dimensional global manifold of flows. We used AUTO to continue the 2PBVPs for the manifold computations in this paper. Four case studies illustrate the fruitful interplay between advancing the reach of the numerical methods and developing new dynamical systems theory.

This paper is organised as follows. In Section 2 we consider stable and unstable invariant manifolds, that is, manifolds that are globally invariant under the flow of the vector field and, either in forward or in backward time, converge to compact invariant objects, such as equilibria and periodic orbits. As specific examples, we consider the stable manifold of the origin in the Lorenz system in Section 2.1 and, in a more applied context in Section 2.2, the interpretation of a stable manifold as an isochrone for a particular phase point along a periodic orbit. In Section 3, we consider invariant manifolds as a tool to explain the effects of finite-time perturbations. In the example in Section 3.1, which is related to the notion of isochrones, we predict a delay or advance of the phase in response to a short-time perturbation. We then consider excitability in Section 3.2, and compute the excitability threshold in the context of a system for which no saddle equilibria or other saddle invariant manifolds are present. We conclude this review in Section 4 with a brief

discussion that also mentions some directions of further research.

2. Stable and unstable manifolds

Stable and unstable manifolds of equilibria, periodic orbits, or other compact normally hyperbolic invariant manifolds of saddle type are an important part of the so-called *skeleton* of a dynamical system. While the attractors organise the eventual, asymptotic behaviour of the system, stable and unstable manifolds describe the global structure of the system, dictating which initial condition goes where, and in what manner.

To fix ideas and notation, let us restrict to vector fields from now on and consider global invariant manifolds of equilibria or periodic orbits. Recall that an equilibrium p is hyperbolic if all eigenvalues of the Jacobian matrix evaluated at p have non-zero real part; similarly, a periodic orbit Γ is hyperbolic if all Floquet multipliers of the linearisation have magnitudes different from 1, except for the Floquet multiplier associated with the direction tangent to Γ; we refer to [46] for details. The stable manifold of p or Γ, denoted $W^s(p)$ or $W^s(\Gamma)$, consists of all trajectories of the flow that converge to p or Γ in forward time; the unstable manifold of p or Γ, denoted $W^u(p)$ or $W^u(\Gamma)$, is its stable manifold when considering the time-reversed flow. The Stable Manifold Theorem [62] guarantees the existence of local (un)stable manifolds of hyperbolic equilibria and periodic orbits associated with their (un)stable eigenvalues or Floquet multipliers, and these manifolds can be extended globally by the flow in either forward or backward time. Furthermore, these manifolds are as smooth as the vector field itself, and they are tangent to the manifolds of the corresponding linearisation.

From these definitions, we deduce that a one-dimensional stable or unstable manifold of an equilibrium p of a vector field consists of two trajectories; each trajectory converges to p in forward or backward time, in a direction tangent to the eigenvector associated with the (strong) stable or unstable eigenvalue, such that the two trajectories together with p form a single smooth (immersed) manifold [62]. From a computational point of view, it is straightforward to compute such one-dimensional manifolds: by selecting an initial point along the appropriate eigenvector at a small distance from p, integration backward (for the stable manifold) or forward in time (for the unstable manifold) generates an orbit segment as an approximation of an arbitrarily long first piece of the manifold. Such an integration produces an ordered list of suitably distributed points on this first piece of the manifold, allowing for its straightforward visualisation as a smooth curve.

A two-dimensional (un)stable manifold, on the other hand, is a lot more difficult to compute and visualise. The challenge lies in the fact that the manifold is now a surface formed by a one-parameter family of trajectories. Hence, a computational method must include instructions how to generate a suitable mesh representation of this surface. Perhaps the simplest approach for designing an algorithm to compute two-dimensional (un)stable manifolds is to select (discretised) orbit segments from the one-parameter family that defines the manifold. Here, a first orbit segment

is computed in the same way as for one-dimensional manifolds, by integration up to the time or length required. Continuation can then be used to follow this first orbit segment as its starting point is varied along a one-dimensional curve in the two-dimensional eigenspace; additional orbit segments are selected from the family as dictated by the spacing between them. This approach often requires a post-processing step of remeshing to visualise the surface. The complementary approach is to ignore the dynamics on the manifold and view it geometrically, for instance, as a family of geodesic level sets. In this case, the mesh is generated as a growing structure based on geometric features, and this aspect can be used for direct visualisation; the disadvantage is that the dynamics on the manifold may cause geometric obstructions, e.g., when there exists a connecting orbit from one equilibrium or periodic orbit to another. We refer to the survey paper [45] for more details on these two (and other) approaches.

In the case studies presented here, we use both approaches, and each uses a formulation via two-point boundary value problems (2PBVP) that are solved by one-parameter continuation with the 2PBVP solver AUTO [16, 17]. We compute a finite set of (discretised) geodesic level sets with the algorithm from [42, 43] if we are interested in the two-dimensional manifold as a surface; this method generates a mesh with good geometric properties and allows for elaborate visualisation. We compute a one-parameter family of orbit segments [44, 45] if we are interested in how a manifold intersects another two- (or higher-)dimensional object, such as a plane or a sphere. Here, we compute the orbit segments up to this intersection and then consider and plot their end points; the orbit segments are selected based on a maximum distance between them, and so the end points give a good mesh representation of the intersection curves.

In the next sections we show how these computational methods can be employed to help understand the topological and geometric nature of the dynamics of a given system. In particular, they allow us to gain insights into different aspects of global dynamics, and we are even able to formulate precise conjectures based on our numerical findings.

2.1. The Lorenz manifold. As the leading example, we consider the stable manifold of the origin of the Lorenz equations. Recall that Lorenz introduced these equations as a much simplified model of convection in the atmosphere [48]. They take the form of three ordinary differential equations,

$$\left\{ \begin{array}{rcl} \dot{x} &=& \sigma\,(y-x), \\ \dot{y} &=& \varrho\,x - y - x\,z, \\ \dot{z} &=& x\,y - \beta\,z. \end{array} \right. \tag{1}$$

Lorenz used the classical values $\sigma = 10$, $\varrho = 28$ and $\beta = 8/3$ as representative parameters. The famous butterfly attractor is the associated globally attracting chaotic set. Note that the origin $\mathbf{0}$ is always an equilibrium of system (1), and it is of saddle type for the classical parameter values. There are two further, symmetrically-related equilibria, denoted $p^{\pm}$ that lie at the centres of the 'wings' of the butterfly attractor. The origin is hyperbolic with one unstable and

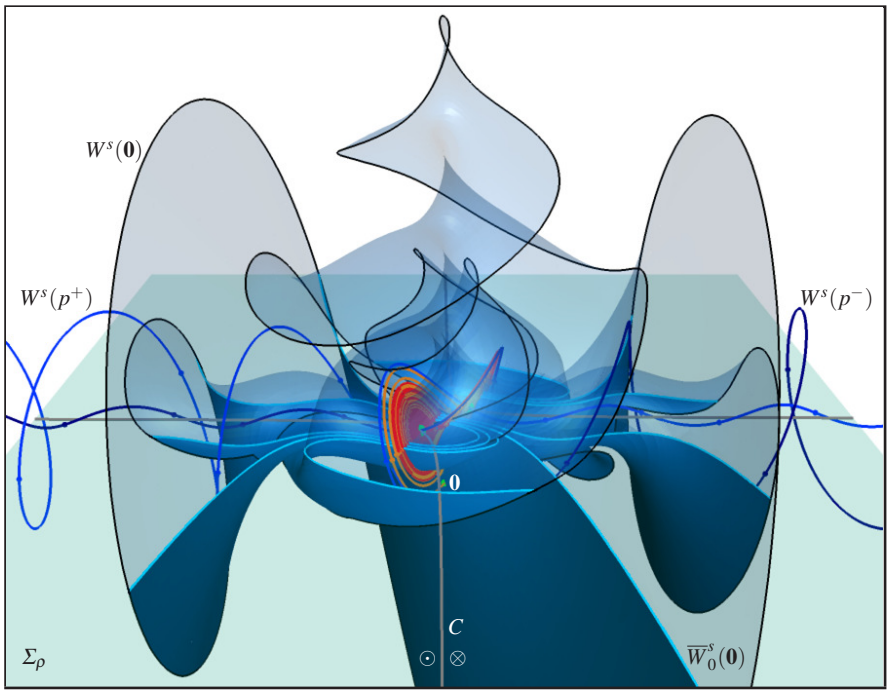

Figure 1. The Lorenz manifold $W^s(\mathbf{0})$, computed up to geodesic distance 162.5, and its intersection with the plane Σ_ϱ; the section Σ_ϱ and the part of $W^s(\mathbf{0})$ above it are rendered transparent. Also shown are the equilibria $\mathbf{0}$ and $p^\pm$, the one-dimensional manifolds $W^u(\mathbf{0})$ and $W^s(p^\pm)$, and the tangency locus C on Σ_ϱ. Reproduced from Osinga, Krauskopf, Hittmeyer, "Chaos and wild chaos in Lorenz-type systems," in Z. Al-Sharawi, J. Cushing and S. Elaydi (eds.) *19th Conference on Difference Equations and Applications* (in press), with permission from Springer-Verlag; see [59, Figure 4].

two stable eigenvalues, which means that it has a one-dimensional unstable and a two-dimensional stable manifold. The equilibria $p^\pm$ each have a pair of complex conjugate unstable eigenvalues, with corresponding two-dimensional unstable manifolds, and one stable eigenvalue, with associated one-dimensional stable manifold. The two-dimensional stable manifold of the origin received its name Lorenz manifold in the survey paper [45] where all contributors used it as their test-case example. From a computational point of view, it is challenging to compute the Lorenz manifold, because there is an order of magnitude difference between the two stable eigenvalues. This means that, locally near the origin, a small disk will quickly transform into an elongated ellipse when carried by the flow backward in time. The nonlinear terms do not balance this effect, so that it is very hard to design algorithms that construct a high-quality mesh on the surface.

Figure 1 shows the Lorenz manifold $W^s(\mathbf{0})$ computed as a surface, that is, computed as a family of geodesic level sets [42, 43]. The outer boundary corresponds

to the approximate geodesic level set at distance 162.5. The surface $W^s(\mathbf{0})$ is intersected with the plane $\Sigma_\varrho = \{z = \varrho - 1 = 27\}$, and the part of $W^s(\mathbf{0})$ that lies above Σ_ϱ, as well as Σ_ϱ itself, is rendered transparent. In this way, we can see the three equilibria $\mathbf{0}$ and $p^\pm$, with their one-dimensional manifolds: the unstable manifold $W^u(\mathbf{0})$ of $\mathbf{0}$ and the stable manifolds $W^s(p^\pm)$ of $p^\pm$. The intersection curves and points of these manifolds with Σ_ϱ are also indicated. The plane Σ_ϱ is the Poincaré section that was used to analyse the nature of the dynamics on the attractor, which is believed to be the closure of $W^u(\mathbf{0})$. The return map is typically defined on the part in between $p^\pm$, where the flow points down from Σ_ϱ. The two hyperbolic curves denoted C separate this region from the regions where the flow points up; the flow is tangent to Σ_ϱ on C. The restriction of this return map to the Lorenz attractor can be approximated by a one-dimensional map, for which it is relatively straightforward to prove that it has chaotic dynamics [1, 30, 77]. The proof that the Lorenz attractor is indeed chaotic was completed only in 1999, and required computer assistance in the form of interval arithmetic [73, 76]. The reduction to a one-dimensional map requires the existence of a (one-dimensional) invariant foliation on Σ_ϱ that is transverse to the Lorenz attractor. We can see a few of the leaves in this foliation, namely, the intersection curves $\overline{W}^s(\mathbf{0}) := W^s(\mathbf{0}) \cap \Sigma_\varrho$; see [59] for more details.

The Lorenz manifold is a complicated surface. It cannot intersect (contain) the one-dimensional manifolds $W^s(p^\pm)$, and for the classical parameter values, it also does not intersect $W^u(\mathbf{0})$. In particular, due to the spiralling nature of $W^u(\mathbf{0})$ (and the attractor), $W^s(\mathbf{0})$ winds in a helical manner around the z-axis, which is contained in $W^s(\mathbf{0})$, while additional helices are formed in symmetric pairs very close to but off the z-axis. At the same time, $W^s(\mathbf{0})$ spirals around $W^s(p^\pm)$. Over the years, the challenge of computing the Lorenz manifold has shifted to the challenge of understanding its geometry. We view the Lorenz manifold as a key object for understanding how the chaotic dynamics manifests itself globally in the Lorenz system (1). Chaotic dynamics is characterised by the presence of sensitive dependence on initial conditions. Two nearby points on the Lorenz attractor quickly diverge under the flow; as a quantative measure, the signature or pattern of oscillations around p^+ and p^- will initially be identical, but after some time the two trajectories will move apart in such a way that the signature will be completely different. Switches between oscillations around p^+ and p^-, respectively, are organised by the close passage near $\mathbf{0}$. More precisely, $W^s(\mathbf{0})$ acts as a local separatrix between trajectories that continue oscillating around p^+, say, and those that switch to oscillating around p^-. Since the Lorenz attractor is a global attractor, any two points in phase space exhibit sensitive dependence on initial conditions, and this is organised globally by $W^s(\mathbf{0})$. This means that the global invariant manifold $W^s(\mathbf{0})$ separates any two points in $\mathbb{R}^3$ and is dense in $\mathbb{R}^3$.

It is mind-boggling to realise that such innocent-looking equations as the Lorenz system (1) give rise to a two-dimensional surface that lies dense in its three-dimensional phase space! This is an actual realised example of a space-filling surface. In order to visualise this topological property, and to study its characteristics further, we consider the intersection of $W^s(\mathbf{0})$ with a sphere S_R that is

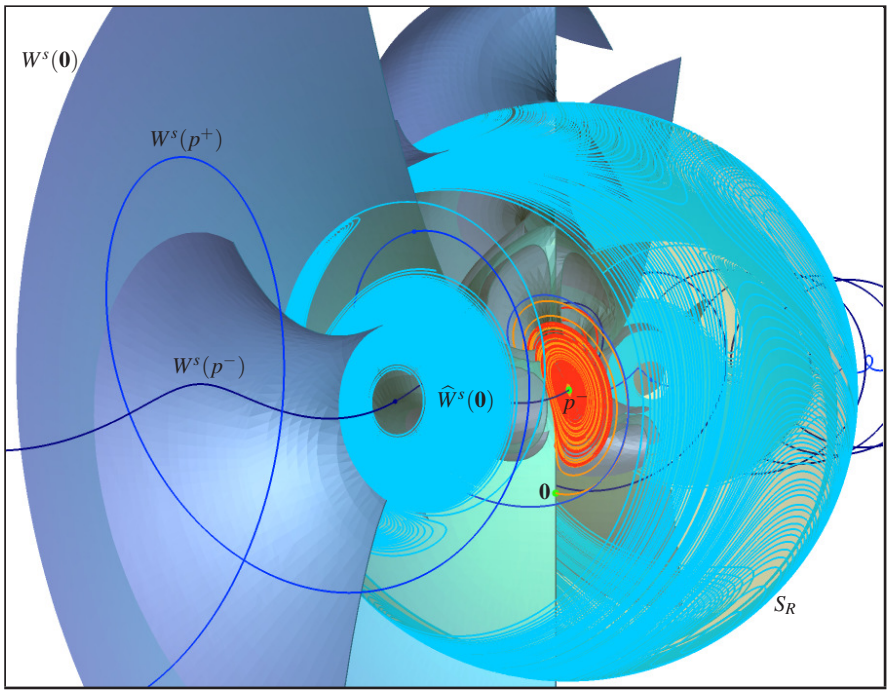

Figure 2. The Lorenz manifold $W^s(\mathbf{0})$ for $\varrho = 28$ intersecting the sphere S_R with $R = 70.7099$ in the set $\widehat{W}^s(\mathbf{0})$; also shown are the equilibria $\mathbf{0}$ and p^- and the one-dimensional manifolds $W^u(\mathbf{0})$ and $W^s(p^\pm)$. Reproduced from Osinga, Krauskopf, Hittmeyer, "Chaos and wild chaos in Lorenz-type systems," in Z. Al-Sharawi, J. Cushing and S. Elaydi (eds.) *19th Conference on Difference Equations and Applications* (in press), with permission from Springer-Verlag; see [59, Figure 2].

centred at the point $(0, 0, 27) \in \Sigma_\varrho$ on the z-axis (the mid-point on the line segment between $p^\pm$) and has large enough radius so that all bounded invariant objects are inside it; more precisely, we choose $R = 70.7099$, which is the distance from the centre of S_R to the second intersection point of the small-amplitude branch of $W^s(p^\pm)$ with Σ_ϱ. Note that S_R is a compact surface so that any intersection curve with $W^s(\mathbf{0})$ must either be a closed curve or an arc with ends that accumulate on some sets, in this case the intersection points $W^s(p^\pm) \cap S_R$. Since $W^s(\mathbf{0})$ is dense in $\mathbb{R}^3$, the intersection curves in $\widehat{W}^s(\mathbf{0})$ must densely fill S_R.

Figure 2 shows $W^s(\mathbf{0})$ intersected with the sphere S_R. To highlight the situation on and inside S_R, only one half of $W^s(\mathbf{0})$ is shown, corresponding to the part that lies in the half space $\{y \geq 0\}$; the sphere S_R is rendered transparant. Many more curves in $\widehat{W}^s(\mathbf{0})$ are shown than those generated by the computed part of the surface $W^s(\mathbf{0})$. Indeed, the curves in $\widehat{W}^s(\mathbf{0})$ were computed directly, using the continuation of the family of trajectories that start on S_R and end on a small ellipse

around $\mathbf{0}$ in the linear stable eigenspace of $\mathbf{0}$; the selected curves are associated with trajectories that satisfy these boundary conditions with a given maximal integration time [19]. The relatively large unfilled region on S_R shown in Figure 2 would be filled eventually, but only when an extremely large maximal integration time is used; two nearby points in these regions, while converging quickly to the Lorenz attractor, will take a comparatively large time to separate. Note the single curve that crosses through the middle of this region; it is the first intersection of $W^s(\mathbf{0})$ with S_R, that is, trajectories starting from points on this curve flow straight to $\mathbf{0}$ without excursions around p^+ or p^-. Hence, the unfilled region is directly related to the fact that trajectories on the Lorenz attractor visit a small neighbourhood of $\mathbf{0}$ far less frequently than similarly small neighbourhoods elsewhere on the Lorenz attractor [70, Appendix F]. Figure 2 also illustrates the structure of $\widehat{W}^s(\mathbf{0})$; the computed curves in $\widehat{W}^s(\mathbf{0})$ are the first of this set of curves that fills S_R densely, and they show that this process is taking place in a certain order associated with a Cantor set; see [19, 59] for more details.

The study of the Lorenz manifold is ongoing, with a focus on the transitions that occur en route to chaos as a parameter is varied; often, ϱ is varied, which is proportional to the Rayleigh number of the convection [48]. For ϱ small enough, there is no chaotic dynamics. After a first homoclinic bifurcation, called the homoclinic explosion point, a so-called pre-turbulent regime is created, where a chaotic saddle is present; this first transition has been widely studied, for example, in [2, 18, 19, 38, 39, 40, 51, 52, 53, 64, 65, 70]. For details on the transition from pre-turbulent to turbulent dynamics, see also [18, 26, 80]; for more recent developments, see [13].

2.2. Isochrones. Isochrones were introduced in 1974 by Winfree [78] to characterise the behaviour of an oscillating system subjected to a brief external stimulus; the same external stimulus can have different effects depending on when it is applied. Such studies are useful, for example, to understand how signalling in neuronal networks is organised. Conceptually, the idea is very simple: the oscillations in the model are generated by an attracting periodic orbit Γ, which is typically assumed to be the only attractor in the system; any perturbation away from the periodic orbit, will result in a transient response that converges back to Γ, but perhaps with a different phase as before. The isochrones foliate the basin of attraction of Γ in such a way that points on the same isochrone converge to Γ with the same phases. Guckenheimer [28] in a follow-up paper from 1975 explained that isochrones are nothing other than the pointwise stable manifolds of Γ. This means that each ischrone is invariant under the time-T map, where T is the period of Γ, and manifold theory can be used to show that isochrones must, therefore, be as smooth as the vector field itself and tangent to the linear stable eigenbundle of Γ [33].

From a geometric point of view, the isochrones form a nice manifold family that foliates the basin of attraction such that all isochrones accumulate on each other near the basin boundary. Winfree already realised this [25, 79], and studied the accumulation of one-dimensional isochrones in the two-dimensional FitzHugh–Nagumo system [24, 54] onto a repelling equilibrium enclosed by the attracting periodic orbit. Winfree expected to be able to compute the isochrones and visualise their geometry spiralling towards this repelling equilibrium, but to his surprise, he encountered serious numerical accuracy issues that could not be overcome at the time [79].

Isochrones have recently enjoyed a new surge of interest, fuelled in part by developments requiring controlled positioning onto specific isochrons. Numerous examples can be found in the context of biological applications, such as neuronal models, where the external stimulus represents a current injection coming from a large underlying neuronal network [23]. However, isochrones are also studied, for example, when regulating synchronisation of power networks that contain a large number of small energy generators, such as wind mills; see [47, 50, 60] for references. These important applications go hand in hand with a renewed interest in the development of appropriate numerical methods to compute isochrones [22, 31, 32, 37, 47, 49, 60, 69, 72]. In particular, we have overcome the accuracy issues reported by Winfree and are now able to compute the isochrones of the FitzHugh–Nagumo system reliably [47].

To illustrate some of these recent results, and discuss the difficulties encountered, we consider here a Hodgkin–Huxley model [35] that is reduced to the two-dimensional form studied in [60]. The model is described by the following system of two equations in terms of the membrane potential V and one of the gating variables n,

$$\left\{ \begin{array}{rcl} \dot{V} & = & -[I_{\mathrm{Na}} + I_{\mathrm{K}} + I_{\mathrm{Leak}}] + I_{\mathrm{app}}, \\ \dot{n} & = & \alpha_n(V)\,(1-n) - \beta_n(V)\,n. \end{array} \right. \tag{2}$$

Here, the different currents are given by

$$\begin{array}{rcl} I_{\mathrm{Na}} & = & g_{\mathrm{Na}}\,[m_\infty(V)]^3\,(0.8-n)\,(V-V_{\mathrm{Na}}), \\ I_{\mathrm{K}} & = & g_{\mathrm{K}}\,n^4\,(V-V_{\mathrm{K}}), \\ I_{\mathrm{Leak}} & = & g_{\mathrm{L}}(V-V_{\mathrm{L}}), \end{array}$$

and I_{app} is the applied current to stimulate the system so that an attracting periodic exists; we use $I_{\mathrm{app}} = 10$ throughout. The so-called quasi-steady-state function $m_\infty(V)$ is derived from the equilibrium assumption of a second gating variable m and is given by an equation of the same form as for n, that is,

$$m_\infty(V) = \frac{\alpha_m(V)}{\alpha_m(V) + \beta_m(V)}.$$

The functions $\alpha_j(V)$ and $\beta_j(V)$, with $j = n, m$ have the form

$$\alpha_j(V) = \frac{a_j(V+V_j)}{1-\exp[-(V+V_j)/k_j]} \quad \text{and} \quad \beta_j(V) = b_j \exp\left(\frac{-(V+E_j)}{\tau_j}\right).$$

$g_{\mathrm{Na}} = 120.0$			$g_{\mathrm{K}} = 36.0$		$g_{\mathrm{Leak}} = 0.3$
$V_{\mathrm{Na}} = 50.0$			$V_{\mathrm{K}} = -77.0$		$V_{\mathrm{L}} = -54.4$
$a_n = 0.01,$	$V_n = 55.0,$	$k_n = 10.0$	$b_n = 0.125,$	$E_n = 65.0,$	$\tau_n = 80.0$
$a_m = 0.1,$	$V_m = 55.0,$	$k_m = 10.0$	$b_m = 4.0,$	$E_m = 65.0,$	$\tau_m = 18.0$

Table 1. Parameters used in the two-dimensional reduced Hodgkin–Huxley model (2).

The particular constants used in this example are given in Table 1.

System (2) evolves on two different time scales; the membrane potential varies fast over a range of order $O(10^2)$, while n, which represents a fraction of open potassium channels, varies slowly over a unit range. While this time-scale separation is not made explicit in the model, one can see it in its spiking behaviour: the time series in V of the attracting periodic orbit Γ of this system has a long subthreshold plateau followed by a rapid large-amplitude spike. One main interest in such systems arises from the question whether it is possible to elicit a spike from the system via a small perturbation from an arbitrary point along the subthreshold plateau. It is generally believed that such a pertubation need only bring the system to a high enough level for V, the precise value of which is called the *spiking threshold*.

Figure 3 shows Γ together with 100 isochrones. The isochrones are distributed uniformly in time along Γ. This means that most isochrones are located on the subthreshold part, which is the lower, approximately horizontal segment of the closed (grey) curve in Figure 3(a). The isochrones are coloured according to a (cyan-to-magenta) colour gradient, starting from the maximal point on Γ (with respect to V), in the (clockwise) direction of the flow. Any perturbation away from Γ will land on a particular isochrone and relax back to Γ in phase with the point on Γ associated with this isochrone. The colour coding seems to reveal a clear spiking threshold, where all isochrones appear to align with each other. We focus on the situation near $n = 0.525$ and zoom into a neighbourhood of the perceived spiking threshold for this n-value, as shown in Figure 3(b). Here, we see that the isochrones do not merely align, but form a much more complicated structure, where each isochrone passes $n = 0.525$ several times while preserving its order in the foliation. This means that a perturbation close to the perceived spiking threshold could result in any arbitrary phase shift and the relationship between the size of the perturbation and the resulting phase shift, at least in this region of sensitivity, is highly nontrivial.

The characterisation of this stretched region of extreme phase sensitivity is related to the accumulation of isochrones near the basin boundary. Due to the two-dimensional nature of the flow, the periodic orbit Γ encloses an equilibrium at $(n, V) \approx (0.4026, -59.61)$, which is repelling. The enlargement in Figure 3(c) illustrates the intricate spiralling nature of the isochrones accumulating onto this equilibrium. The extreme phase sensitivity, not only near the equilibrium, is organised by the repelling slow manifold associated with the repelling branch of the cubic critical manifold; see [47, 60] for more details.

The computation of the isochrones uses a two-point boundary value set-up

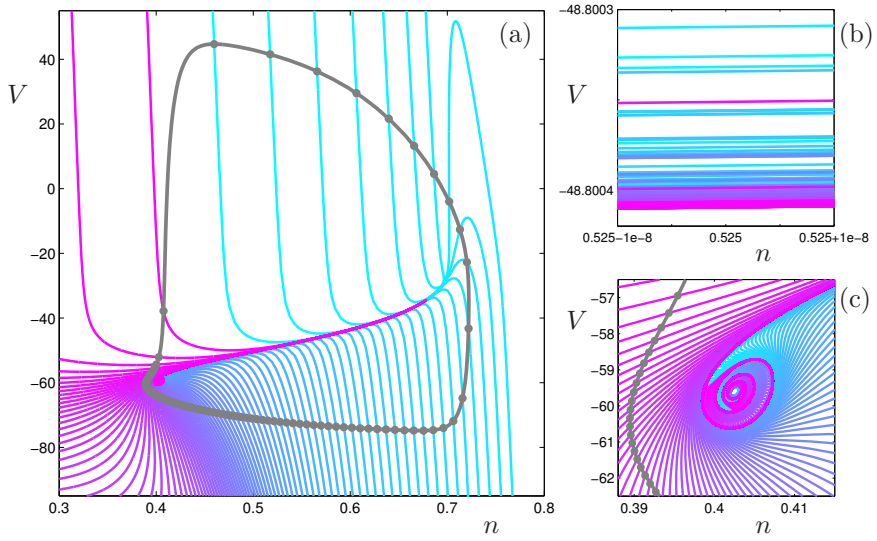

Figure 3. Extreme phase sensitivity near the excitability threshold in the reduced Hodgkin–Huxley model (2). Shown are the isochrones of 100 points along the periodic orbit (grey) that are distributed uniformly in time. Panel (b) shows the phase sensitivity in an enlargement near $n = 0.525$; and panel (c) illustrates how the isochrones organise the phase sensitivity near the equilibrium at $(n, V) \approx (0.4026, -59.61)$.

that is essentially the same as a stable-manifold calculation [47, 60]. We continue a one-parameter family of orbit segments with integration times equal to integer multiples of the period of Γ. By restricting one end point to a small interval along the linear stable eigendirection at a point $\gamma \in \Gamma$, the points at the other end of such a family of orbit segments forms the isochrone associated with γ. The resulting algorithm computes the isochrone as a curve parametrised by arclength and avoids the numerical accuracy issues reported by Winfree [79]. The continuation of the 2PBVP can trace the isochrone through regions of extreme phase sensitivity, because the entire orbit segments associated with ends points on different isochrones that are indistinguishable in this region, remain well separated.

3. Slow manifolds and transient effects

The example of the Hodgkin–Huxley model (2) in Section 2.2 illustrates that an excitability threshold can be much more complicated than generally assumed. Moreover, it highlights the need for a deeper mathematical understanding of bursting behaviour. The analysis of bursting goes back to the 1980s when Rinzel, at the 1986 ICM, proposed a simple approach to classifying bursting mechanisms in excitable systems [67]. Rinzel utilises the fact that excitable systems typically feature

variables that evolve on rather different time scales. More precisely, the model can be written as

$$\begin{cases} \dot{x} = \quad f(x,y), \\ \dot{y} = \varepsilon\, g(x,y), \end{cases} \tag{3}$$

where $x \in \mathbb{R}^n$ and $y \in \mathbb{R}^m$, with $n, m \geq 1$. Here, $0 < \varepsilon \ll 1$ represents the single time-scale separation between y and x. If we take the singular limit $\varepsilon \to 0$ then y becomes a vector of parameters and the equation for x, called the fast subsystem, exhibits dynamics that depends on the choice for y. Rinzel discusses the case with $m = 1$ in detail. Bursting, or spiking, occurs when the one-parameter bifurcation diagram in y of the fast subsystem exhibits hysteresis, and the y-nullcline is positioned such that the slow evolution of y causes an oscillation of y across this hysteresis regime. This idea of freezing the slow variable can even be used when ε is not explicitly present in the equations. For example, in the reduced Hodgkin–Huxley model (2), the variable V was found to be at least 100 times faster than n. Hence, one can view n as a parameter and analyse the one-dimensional fast subsystem given by the equation for V. Three equilibria co-exists for n approximately in the interval $[0.3085, 0.7072]$, both end points of which are fold points; the branches corresponding to the highest and lowest V-values are stable. Furthermore, n is decreasing on the lower branch and increasing on the upper branch in the hysteresis interval. One concludes that the full two-dimensional system exhibits a relaxation oscillation that traces the two branches of stable equilibria, interspersed by two (fast) jumps approximately at the fold points; the relaxation oscillation is the (gray) periodic orbit shown in Figure 3(a).

Different bursting patterns arise when there are additional bifurcations along the branches of equilibria. For example, multi-spike bursting oscillations arise when the upper branch includes a Hopf bifurcation, so that the fast subsystem exhibits periodic oscillations over a range of y-values; this case was already discussed in [67], but see also the example in the next section, where the fast subsystem undergoes a subcritical Hopf bifurcation, which gives rise to a family of unstable (saddle) periodic orbits, but nevertheless, generates a multi-spike burst. Bursting behaviour can also be organised by a slow-fast system with two or more slow variables; see [14] for a detailed discussion and literature overview.

The case studies presented in the following two sections are using the same ideas as introduced by Rinzel [66, 67], but utilise recent developments in manifold computations to enhance this approach and enlarge it applicability.

3.1. Predicting the phase response. In complete analogy to the two-dimensional reduced Hodgkin–Huxley model (2), we consider, here, the problem of phase resetting for a model of a pituitary cell. The model is four dimensional and uses the same Hodgkin–Huxley formalism as described in detail for system (2). One equation is for the membrane potential V, two are for channel gating variables n and m, and one is for calcium balance in the cell body:

$$\left\{\begin{array}{rcl} C_m\dot{V} &=& -[I_{\mathrm{CaL}} + I_{\mathrm{CaT}} + I_{\mathrm{K}} + I_{\mathrm{KCa}} + I_{\mathrm{Leak}}] + I_{\mathrm{app}}, \\ \dot{n} &=& \dfrac{n_\infty(V) - n}{\tau_n}, \\ \dot{m} &=& \dfrac{m_\infty(V) - m}{\tau_m(V)}, \\ \dot{Ca} &=& J_{\mathrm{exchange}} + f\,\beta\,(J_{\mathrm{influx}} - J_{\mathrm{efflux}}). \end{array}\right. \tag{4}$$

A full description of the model can be found in [71]; we only mention here that $I_{\mathrm{app}} = 0$ by default; it is only used for perturbing the spiking behaviour of the cell. Rather than eliciting a single spike, system (4) with $I_{\mathrm{app}} = 0$ exhibits a series of spikes during the active phase of the periodic orbit Γ. As for the reduced Hodgkin–Huxley model (2), most of the time is spent on a subthreshold plateau, and one is interested in understanding the response to perturbations away from this subthreshold segment of Γ. One particular difficulty with this model is to achieve an 'active' phase shift, in the sense that the perturbation brings the membrane potential up into the active phase and gives rise to a spike train before V drops back down to subthreshold levels.

System (4) has three different time scales: just as for the reduced Hodgkin–Huxley model (2), the membrane potential V varies on a much faster time scale than the two gating variables n and m. The calcium concentration varies even more slowly than the gating variables and it is this variable Ca that is singled out in the geometric singular perturbation theory, leaving a three-dimensional fast subsystem for analysis. The (V, n, m)-subsystem has two families of Ca-dependent stable equilibria, denoted e_{H} and e_{L} for the active and silent phases, respectively. The branch e_{L} exists only for large enough Ca, and coexists with a family e_{M} of saddle equilibria that meet at a fold. The branch e_{H} destabilises in a subcritical Hopf bifurcation for a Ca-value to the right of this fold point. Hence, there is a Ca-interval for which the two stable equilibria e_{H} and e_{L} coexist. The situation seems similar to the case discussed in Section 2.2, but the Hopf bifurcation gives rise to a family of saddle periodic orbits Γ_{H} that coexist with e_{H} and e_{L} for large enough Ca in the bistability interval.

We use the analysis of the fast subsystem to explain the difficulty in achieving an active phase shift. To this end, we focus on a single Ca-value, namely $Ca = 1$, for which all three equilibria as well as the saddle periodic orbit are present. A perturbation in the form of a current I_{app} is applied during the silent phase, such that $Ca = 1$, that is, (approximately) from the equilibrium e_{L}. We assume that the transient effects caused by the perturbation are of such a short-time nature that Ca remains practically at 1. If this is indeed the case, then I_{app} must be such

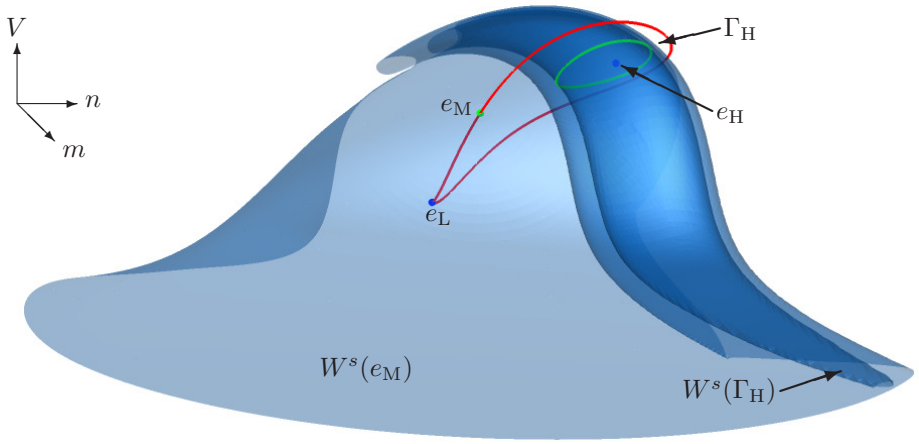

Figure 4. Stable manifolds of the equilibrium $e_{\rm M}$ and periodic orbit $\Gamma_{\rm H}$ of the fast subsystem of (4) with $Ca = 1$.

that $e_{\rm L}$, which for this new value of $I_{\rm app}$ is most certainly no longer an equilibrium, flows towards the basin of attraction of $e_{\rm H}$. Again, we assume that this transient motion is so fast that Ca hardly changes. As soon as the basin boundary is crossed, $I_{\rm app}$ can be switched off and we may assume that the dynamics will switch back to its unperturbed course with the required phase shift. Figure 4 shows the equilibria and periodic orbit of the fast subsystem for $Ca = 1$. Also shown are the two-dimensional stable manifolds $W^s(e_{\rm M})$ and $W^s(\Gamma_{\rm H})$ of $e_{\rm M}$ and $\Gamma_{\rm H}$, respectively. The manifolds $W^s(e_{\rm M})$ and $W^s(\Gamma_{\rm H})$ were computed with the same method described in Section 2.1. The basin boundary of $e_{\rm H}$ is the separatrix $W^s(\Gamma_{\rm H})$, but $W^s(e_{\rm M})$ also acts as a kind of separatrix, because a crossing of $W^s(e_{\rm M})$ leads to one or more spikes before relaxation back to $e_{\rm L}$.

For $I_{\rm app} > 0$ small enough, the fast subsystem has a similar set of three equilibria and one periodic orbit. Hence, for $I_{\rm app} > 0$ small enough, the flow will simply push $e_{\rm L}$ to the corresponding (lower) stable equilibrium for the new value of $I_{\rm app}$; this will not lead to an active phase shift. For $I_{\rm app} > 0$ large enough, however, only one equilibrium exists, which can be associated with the active phase. For example, if $I_{\rm app} = 6.69$, a unique attracting equilibrium exists near $e_{\rm H}$. Unfortunately, this equilibrium lies outside the basin of attraction of $e_{\rm H}$. This is the case for all values of $I_{\rm app}$ for which only one equilibrium exists. Figure 5 illustrates the possible transient behaviour while $I_{\rm app} = 6.69$. The trajectory departs from $e_{\rm L}$ and spirals towards the attractor for this $I_{\rm app}$-value. On its way, $W^s(\Gamma_{\rm H})$ is crossed four times, creating two short time windows in which the applied current could be reset to $I_{\rm app} = 0$ and an active phase shift could possibly occur.

From this analysis we predict two successful perturbation protocols, both of which require holding $I_{\rm app}$ at a positive value for a certain (nontrivial) amount of time. Subsequent dynamic testing of these perturbation protocols for the full

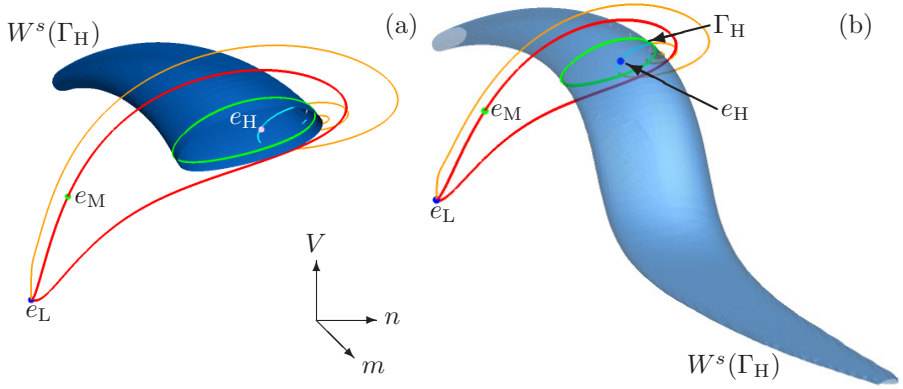

Figure 5. Starting from e_L, an applied current $I_{app} = 6.69$ results in two excursions inside the basin of attraction of e_H while spiralling towards an attractor outside this basin.

four-dimensional system indeed showed that an active phase shift can be achieved only for two particular segments in the silent phase. Perhaps more importantly, this research provided the precise ranges of values to use for I_{app} and the time duration befor reset to $I_{app} = 0$; until these results were known, researchers had been unable to find any kind of active phase reset for this type of pituitary cell model. We refer to [71] for more details.

It is interesting to note that the stable manifold of the coexisting saddle equilibrium e_M controls the number of spikes seen in a transient burst. The accumulation of $W^s(e_M)$ onto $W^s(\Gamma_H)$ occurs in the fast subsystem, but it is very similar to the isochrones accumulating onto a slow manifold, which occurs in the full system; for example, see the structure of the isochrones for the reduced Hodgkin–Huxley model in Section 2.2. As yet, there are no good methods available to compute higher-dimensional isochrones and the precise analogy remains a challenging area of research.

3.2. Excitability thresholds. The idea of using an applied current to elicit a spike or spike train from the model can be further refined to establish exactly how many spikes will be generated after such a perturbation. In [56, 57] we considered a five-dimensional model that closely mimics the bursting behaviour of a pyramidal neurone in the so-called CA1 and CA3 regions of the hippocampus. Such CA1/CA3 cells are known to play an important role in the onset of Alzheimer's disease [5, 11, 55]. In experiments, these cells are subjected to a short current injection and the response of their membrane potential is recorded. A model for such a cell, constructed with the Hodgkin–Huxley formalism, offers insight into how the different currents bring about the various responses. Furthermore, the model can give a precise mathematical mechanism explaining how new spikes in the spike train are added when a parameter is varied.

The model combines equations for the membrane potential and four gating variables, corresponding to activation of slow inward and fast and slow outward currents, and inactivation of the slow inward current. Here, we consider only the model for a CA3 pyramidal neurone; the model for the CA1 neurone can be obtained by using a different set of parameters [55]. The parameters are such that the system is at its resting potential, which is an attracting equilibrium in the model; we refer to [56] for more details on the model equations. We study the transient response of this system when it is perturbed away from the stable equilibrium by an applied current of $20\,\mu\mathrm{A/cm}^2$ for a duration of only 3 ms. When the conductance parameter g_{SI} corresponding to the slow inward current is varied, this same short current-injection protocol leads to a variety of responses. More precisely, the strength and duration of the applied current is chosen such that, over a range of g_{SI}-values, the perturbation pushes the system past the top of a first spike; the difference between responses is characterised by what happens after the current injection, during the transient phase when the applied current is switched off and the system relaxes back to its stable equilibrium. Figure 6 shows three such responses, namely, for $g_{\mathrm{SI}} = 0.1$, for which the response immediately relaxes back to equilibrium, $g_{\mathrm{SI}} = 0.5$, for which the relaxation occurs via a non-monotonic route, and $g_{\mathrm{SI}} = 0.6\,\mathrm{mS/cm}^2$, for which the response exhibits two further spikes before relaxation back to equilibrium.

The transformation from a single-spike to a three-spike response occurs via a spike-adding sequence, but the g_{SI}-interval of the two-spike response is very small and an example of such a response is not shown in Figure 6. In fact, experimental findings also report that it is difficult to obtain a two-spike response [11]. In order to investigate the mechanism underlying the spike-adding behaviour, at least from a mathematical point of view, we use geometric singular perturbation theory by utilising the different time scales in the model. Both the gating variables m_{SO} and h_{SI}, corresponding to activation of the slow outward current and inactivations of the slow inward current, respectively, are much slower than the other variables. Therefore, we consider the fast subsystem, represented by the membrane potential V, and the gating variables m_{SI} and m_{FO} corresponding to the slow inward and fast outward currents, respectively.

Since we now have two slow variables, the equilibria in this fast subsystem are

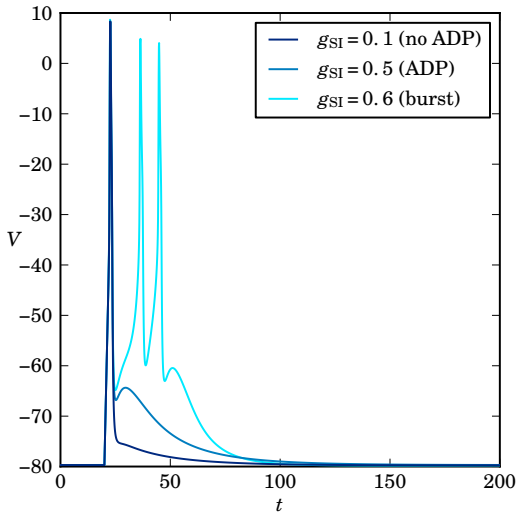

Figure 6. The same short current-injection protocol leads to different responses when a parameter is varied. Reproduced from Nowacki, Osinga, Tsaneva-Atanasova, "Dynamical systems analysis of spike-adding mechanisms in transient bursts," *Journal of Mathematical Neuroscience* **2** (2012): 7, with permission from Springer-Verlag; see [56, Figure 1].

organised in families that form surfaces in the five-dimensional phase space. In fact, they form a single folded sheet, if one allows $h_{\rm SI}$ to attain non-physical values. The lower segment (with respect to V) of this sheet consists of attracting equilibria, one of which corresponds to the stable equilibrium of the full five-dimensional system. The upper segment (with respect to V) is organised in much the same way as for the fast subsystem of (4) in Section 3.1: there exists a curve of subcritical Hopf bifurcations, which give rise to a two-parameter family of saddle periodic orbits. For the CA3 neurone model, this family of saddle periodic orbits undergoes a fold that stabilises the family before ending at a curve of homoclinic bifurcations. Figure 7 shows these two-parameter families of equilibria and maxima and minima of the periodic orbits for $g_{\rm SI} = 0.5615$, which is a special value with respect to the behaviour of the full system, but representative for the geometric organisation of the equilibria and periodic orbits of the fast subsystem. The projection is onto $(h_{\rm SI}, m_{\rm SO}, V)$-space, showing V against the two slow variables $h_{\rm SI}$ and $m_{\rm SO}$. The surface of equilibria is labelled in segments according to the stability changes due to fold or Hopf bifurcations. The lower sheet is labelled S_1^a; past the first fold, — which occurs along a curve with $h_{\rm SI}$ outside its physical range and is not shown in Figure 7, — the equilibria are of saddle type and labelled S_1^r. There are two further folds that occur in quick succession, leading to an attracting segment S_2^a and another saddle segment S_2^r. The upper fold (with respect to V) gives rise to

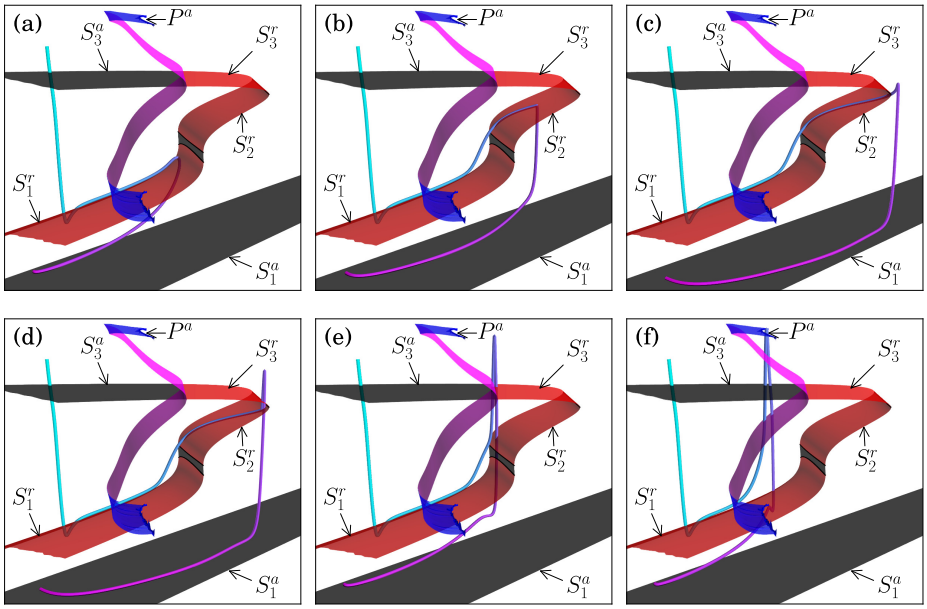

Figure 7. A spike-adding transition for the CA3 pyramidal neurone model with $g_{\rm SI} \approx 0.5615$ increasing over an exponentially small interval. Reproduced from Nowacki, Osinga, Tsaneva-Atanasova, "Dynamical systems analysis of spike-adding mechanisms in transient bursts," *Journal of Mathematical Neuroscience* **2** (2012): 7, with permission from Springer-Verlag; see [56, Figure 5].

a segment for which the equilibria have two unstable eigenvalues, and is labelled S_3^r; the upper attracting segment, on the other side of the Hopf curve, is labelled S_3^a. Similarly, the families of periodic orbits are denoted P^r and P^a.

Overlayed on the two-parameter families of equilibria are orbit segments of trajectories of the full five-dimensional system, starting from the point when the current injection has been switched off. From panels (a) to (f), the conductance $g_{\rm SI} \approx 0.5615$ is increasing, but only over an exponentially small interval; all $g_{\rm SI}$-values round to 0.5615. Figure 7 illustrates the significance of this value $g_{\rm SI} \approx 0.5615$, because in an exponentially small interval near this value, the orbit segment undergoes a dramatic transition that causes the creation of a new spike. While it is hard to see from such three-dimensional projections how this is organised in the five-dimensional phase space, Figure 7 gives a clear impression that the orbit segment tracks the unstable sheets S_1^r and S_2^r during the transition; we checked that this is indeed the case. A new spike is created when, at a special parameter value for $g_{\rm SI}$, the orbit segment does not immediately relax back to S_1^a, but is captured by the sheet S_1^r. At first, the orbit segment tracks S_1^r for only a short while before

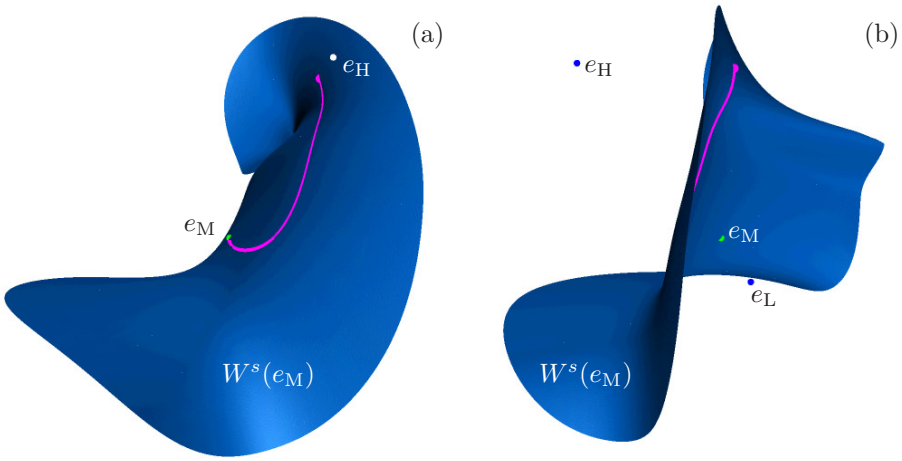

Figure 8. The stable manifold of the saddle equilibrium e_{M} on S_1^r with $h_{\mathrm{SI}} = 0.6865$ and $m_{\mathrm{SO}} = 0.02534$.

dropping down to S_1^a; see Figure 7(a). However, as g_{SI} increases, the orbit segment not only tracks S_1^r, but continues along S_2^r up to its fold with S_3^r before dropping back downd to S_1^a; see Figures 7(b) and (c). The transformation proceeds via the topological change that, after tracking S_1^r and S_2^r, the orbit segment jumps up before dropping down to S_1^a; see Figure 7(d). Subsequently, the tracking along S_1^r and S_2^r is gradually withdrawn, while the jump up develops into a real spike. We remark that the spike-adding transition for the CA3 neurone model is relatively complicated, involving two slow variables and a transition between two saddle-unstable sheets S_1^r and S_2^r. There features are important for the biology and help mimic precise details of the experimental results. However, the minimal ingredients for a spike-adding transition as illustrated in Figure 7 can be provided by a three-dimensional model with a single slow variable; see [61].

The spike-adding transition is initialised at the moment when the perturbation at the end of the short current injection is such that the orbit segment is captured by S_1^r. If we assume that the two slow variables h_{SI} and m_{SO} hardly change, we can illustrate this capture in $(m_{\mathrm{SI}}, m_{\mathrm{FO}}, V)$-space with respect to the fast subsystem. Figure 8 shows two views of the stable manifold of the saddle equilibrium e_{M} on S_1^r for the fast subsystem in $(m_{\mathrm{SI}}, m_{\mathrm{FO}}, V)$-space with $h_{\mathrm{SI}} = 0.6865$ and $m_{\mathrm{SO}} = 0.02534$; in both views, the vertical axis is V. The manifold $W^s(e_{\mathrm{M}})$ separates the basins of attraction of the two stable equilibria e_{L} on S_1^a and e_{H} on S_3^a; compare Figure 7. In the full five-dimensional phase space, $W^s(e_{\mathrm{M}})$ is not a separatrix; it is not even an invariant manifold and e_{L}, e_{M} and e_{H} are not equilibria. We interpret Figure 8 in the following way. A spike-adding transition occurs when the parameter g_{SI} is such that the trajectory perturbed from the stable equilibrium of the full system lands exponentially close to $W^s(e_{\mathrm{M}})$ immediately after the 3 ms current injection. Here, $W^s(e_{\mathrm{M}})$ represents the stable manifold of the

equilibrium $e_{\rm M}$ on S_1^τ that corresponds to the (approximate) $h_{\rm SI}$- and $m_{\rm SO}$-values at the time immediately after the 3 ms current injection. As shown in Figure 8, the trajectory of the full five-dimensional system starts at a point near $e_{\rm H}$, because the perturbation gave rise to a first spike. It lies (approximately) on $W^s(e_{\rm M})$ and, thus, converges to $e_{\rm M}$. Since the fast directions dominate, $h_{\rm SI}$ and $m_{\rm SO}$ hardly change at first, and we can follow the convergence almost up to $e_{\rm M}$ in this 'frozen' image. Close to $e_{\rm M}$, or more precisely, close to S_1^τ, the slow dynamics dominates and the trajectory starts tracking S_1^τ with $h_{\rm SI}$ and $m_{\rm SO}$ varying over a relatively large range; see Figure 7.

The excitability threshold in this system is not organised by the existence of a stable manifold in the full system, associated with a saddle equilibrium or other saddle-type invariant object. The role of the excitability threshold is taken over by unstable (saddle) slow manifolds that exist due to the presence of multiple time scales in the system. As argued here, the spike-adding dynamics is organised by the special events when a perturbation causes a shift exactly onto the stable manifold of a saddle slow manifold. One must be cautious here, because neither slow manifolds nor their stable manifolds are uniquely defined [14, 20]. In our case study, we consider the situation in the singular limit, for which the required stable manifold is uniquely defined, but for the full system, this means that the spike adding will be spread over an exponentially small parameter interval, during which the pertubation causes a shift onto stable manifolds of a family of saddle slow manifolds. The precise nature of such a transition, while observed numerically, has yet to be analysed in detail theoretically.

4. Conclusions

The case studies presented in this paper demonstrated that the continuation of two-point boundary value problems for the computation of global invariant manifolds is a powerful tool for the investigation of practical issues arising in applications, as well as questions in dynamical systems theory. In fact, these methods are so accurate that they allow for detailed quantitative predictions and the formulation of specific conjectures. Computations based on boundary-value-problem formulations can be used widely in dynamical systems; in particular, they are very well suited for the investigation of systems with multiple time scales. Moreover, they allow for a systematic investigation of transient phenomena.

We conclude this paper by mentioning a few directions of future research. In related and ongoing work, we consider the organisation of phase space near global bifurcations, including the Shilnikov bifurcation [4] and homoclinic flip bifurcations [3]. We also want to explore higher-dimensional systems, with a particular focus on hetero-dimensional cycles; an example with explicit equations of a system with hetero-dimensional cycles has only recently been found [81]. Such cycles are known to be related to the existence of wild chaos that can arise in vector fields of dimension at least four [8, 34, 74, 75]. We also continue our study of systems with multiple time scales and are particularly interested in interactions between

slow manifolds and global invariant manifolds of such systems [14]. Furthermore, we would like to characterise the different mechanisms of spike adding in transient bursts [57, 61]. Finally, the computational approach to analyse transient bursts can also be employed in different applications. We are particularly interested in the stability analysis of a structure during an earthquake. The so-called failure boundary in this problem is similar to the excitability threshold studied in this paper. Initial computations that employ continuation of a two-point boundary value problem to find such failure boundaries directly, show that the boundary is formed in a complicated way, composed of piecewise-smooth segments from the solution family [58].

Acknowledgments

The research presented in this paper is the result of several collaborations and I would like to express my sincere gratitude to my coauthors. First and foremost, I thank Bernd Krauskopf for his continued enthusiasm and drive to work with me for almost two decades on many exciting areas of dynamical systems; I am particularly grateful for his detailed comments on a first draft of this paper. I also thank Eusebius Doedel, Arthur Sherman and Krasimira Tsaneva-Atanasova for our fruitful joint research activities that already span more than ten years as well. Bernd and I had the privilege to work with PhD students Pablo Aguirre, Jennifer Creaser, Mathieu Desroches, Peter Langfield, and Stefanie Hittmeyer on the global manifold computations discussed here, and Krasi and I enjoyed working with our PhD student Jakub Nowacki on transient dynamics.

References

[1] Afrajmovich, V. S., Bykov, V. V., Sil′nikov, L. P., The origin and structure of the Lorenz attractor, *Sov. Phys. Dokl.* **22** (1977), 253–255; translation from *Dokl. Akad. Nauk SSSR* **234**(2) (1977), 336–339.

[2] Aguirre, P., Doedel, E. J., Krauskopf, B., Osinga, H. M., Investigating the consequences of global bifurcations for two-dimensional invariant manifolds of vector fields, *Discr. Contin. Dynam. Syst. – Ser. A* **29**(4) (2011), 1309–1344.

[3] Aguirre, P., Krauskopf, B., Osinga, H. M., Global invariant manifolds near homoclinic orbits to a real saddle: (non)orientability and flip bifurcation, *SIAM J. Appl. Dynam. Syst.* **12**(4) (2013), 1803–1846.

[4] Aguirre, P., Krauskopf, B., Osinga, H. M., Global invariant manifolds near a Shilnikov homoclinic bifurcation, *J. Comput. Dynam.* **1**(1) (2014), 1–38.

[5] Andersen, P., Morris, R., Amaral, D., Bliss, T., O'Keefe, J., *The Hippocampus Book.* Oxford University Press, New York, 2007.

[6] Arnol′d, V. I., *Geometrical Methods in the Theory of Ordinary Differential Equations.* Springer-Verlag, Berlin, 2^{nd} edition, 1988.

[7] Ascher, U. M., Christiansen, J., Russell, R. D., Collocation software for boundary value ODEs, *ACM Trans. Math. Software* **7**(2) (1981), 209–222.

[8] Bamón, R., Kiwi, J., Rivera-Letelier, J., Wild Lorenz like attractors, arXiv 0508045 (2006); available at `http://arxiv.org/abs/math/0508045/`.

[9] Beyn, W.-J., Kleinkauf, J.-M., The numerical computation of homoclinic orbits for maps, *SIAM J. Numer. Anal.* **34** (1997), 1207–1236.

[10] Boor, C. de, Swartz, B., Collocation at Gaussian points, *SIAM J. Numer. Anal.* **10**(4) (1973), 582–606.

[11] Brown, J. T., Randall, A. D., Activity-dependent depression of the spike after-depolarization generates long-lasting intrinsic plasticity in hippocampal CA3 pyramidal neurons, *J. Physiol.* **587**(6) (2009), 1265–1281.

[12] Champneys, A. R., Kuznetsov, Yu. A., Sandstede, B., A numerical toolbox for homoclinic bifurcation analysis, *Internat. J. Bifur. Chaos Appl. Sci. Engrg.* **6**(5) (1996), 867–887.

[13] Creaser, J. L., Krauskopf, B., Osinga, H. M., α-flips in the Lorenz system, Preprint of The University of Auckland (2013).

[14] Desroches, M., Guckenheimer, J., Krauskopf, B., Kuehn, C., Osinga, H. M., Wechselberger, M., Mixed-mode oscillations with multiple time scales, *SIAM Review* **54**(2) (2012), 211–288.

[15] Dhooge, A., Govaerts, W., Kuznetsov, Yu. A., MATCONT: A MATLAB package for numerical bifurcation analysis of ODEs, *ACM Trans. Math. Software* **29**(2) (2003), 141–164.

[16] Doedel, E. J., AUTO, a program for the automatic bifurcation analysis of autonomous systems, *Congr. Numer.* **30** (1981), 265–384.

[17] Doedel, E. J., AUTO-07P: Continuation and bifurcation software for ordinary differential equations, with major contributions from Champneys, A. R., Fairgrieve, T. F., Kuznetsov, Yu. A., Oldeman, B. E., Paffenroth, R. C., Sandstede, B., Wang, X. J., Zhang, C. (2007); available at `http://cmvl.cs.concordia.ca/auto/`.

[18] Doedel, E. J., Krauskopf, B., Osinga, H. M., Global bifurcations of the Lorenz manifold, *Nonlinearity* **19**(12) (2006), 2947–2972.

[19] Doedel, E. J., Krauskopf, B., Osinga, H. M., Global invariant manifolds in the transition to preturbulence in the Lorenz system, *Indag. Math. (N.S.)* **22**(3–4) (2011), 222–240.

[20] Dumortier, F., Roussarie, R., *Canard cycles and center manifolds.* Mem. Amer. Math. Soc. **121**, Providence, RI, 1996; with an appendix by Cheng Zhi Li.

[21] Ermentrout, G. B., *Simulating, Analyzing, and Animating Dynamical Systems* (A Guide to XPPAUT for Researchers and Students). SIAM, Philadelphia, 2002.

[22] Ermentrout, G. B., Glass, L., Oldeman, B. E., The shape of phase-resetting curves in oscillators with a saddle node on an invariant circle bifurcation, *Neural Computation* **24**(12) (2012), 3111–3125.

[23] Ermentrout, G. B., Terman, D. H., *Mathematical Foundations of Neuroscience.* Springer-Verlag, New York, 2010.

[24] FitzHugh, R., Impulses and physiological states in theoretical models of nerve membrane, *Biophys. J.* **1**(6) (1961), 445–466.

[25] Glass, L., Winfree, A. T., Discontinuities in phase-resetting experiments, *Amer. J. Physiol.-Regul., Integr. Compar. Physiol.* **246**(2) (1984), R251–R258.

[26] Glendinning, P., Sparrow, C., Local and global behavior near homoclinic orbits, *J. Statist. Phys.* **35** (1984), 645–696.

[27] Govaerts, W., Kuznetsov, Yu. A., Interactive continuation tools, in Krauskopf, B., Osinga, H. M., Galán-Vioque, J. (eds.) *Numerical Continuation Methods for Dynamical Systems*, pp. 51–75. Springer-Verlag, New York, 2007.

[28] Guckenheimer, J., Isochrons and phaseless sets, *J. Math. Biol.* **1**(3) (1975), 259–273.

[29] Guckenheimer, J., Holmes, P., *Nonlinear Oscillations, Dynamical Systems and Bifurcations of Vector Fields*. Springer-Verlag, New York, 2^{nd} edition, 1986.

[30] Guckenheimer, J., Williams, R. F., Structural stability of Lorenz attractors, *Publ. Math. IHES* **50** (1979), 59–72.

[31] Guillamon, A., Huguet, G., A computational and geometric approach to phase resetting curves and surfaces, *SIAM J. Appl. Dynam. Syst.* **8**(3) (2009), 1005–1042.

[32] Gutkin, B. S., Ermentrout, G. B., and Reyes, A. D., Phase-response curves give the responses of neurons to transient inputs, *J. Neurophysiology* **94**(2) (2005), 1623–1635.

[33] Hirsch, M. W., Pugh, C. C., Shub, M., *Invariant Manifolds*. Lecture Notes in Math. **583**, Springer-Verlag, New York, 1977.

[34] Hittmeyer, S., Krauskopf, B., Osinga, H. M., Interacting global invariant sets in a planar map model of wild chaos, *SIAM J. Appl. Dynam. Syst.* **12**(3) (2013), 1280–1329.

[35] Hodgkin, A. L., Huxley, A. F., A quantitive description of membrane current and its application to conduction and excitation in nerve, *J. Physiol.* **117**(4) (1952), 500–544.

[36] Homburg, A. J., Sandstede, B., Homoclinic and heteroclinic bifurcations in vector fields, in Broer, H. W., Takens, F., Hasselblatt, B. (eds.), *Handbook of Dynamical Systems* Vol. **3**, pp. 379–524. North-Holland, Amsterdam, 2010.

[37] Huguet, G., de la Llave, R., Computation of limit cycles and their isochrons: Fast algorithms and their convergence, *SIAM J. Appl. Dynam. Syst.* **12**(4) (2013), 1763–1802.

[38] Jackson, E. A., The Lorenz system: I. The global structure of its stable manifolds, *Physica Scripta* **32**(5) (1985), 469–475.

[39] Jackson, E. A., The Lorenz system: II. The homoclinic convolution of the stable manifolds, *Physica Scripta* **32**(5) (1985), 476–481.

[40] Kaplan, J. L., Yorke, J. A., Preturbulence: A regime observed in a fluid flow model of Lorenz, *Commun. Math. Phys.* **67** (1979), 93–108.

[41] Keller, H. B., Numerical solutions of bifurcation and nonlinear eigenvalue problems, in Rabinowitz, P. H. (ed.) *Applications of Bifurcation Theory*, pp 359–384. Academic Press, New York, 1977.

[42] Krauskopf, B., Osinga, H. M., Two-dimensional global manifolds of vector fields, *CHAOS* **9**(3) (1999), 768–774.

[43] Krauskopf, B., Osinga, H. M., Computing geodesic level sets on global (un)stable manifolds of vector fields, *SIAM J. Appl. Dynam. Sys.* **2**(4) (2003), 546–569.

[44] Krauskopf, B., Osinga, H. M., Computing invariant manifolds via the continuation of orbit segments, in Krauskopf, B., Osinga, H. M., Galán-Vioque, J. (eds.) *Numerical Continuation Methods for Dynamical Systems*, pp 117–154. Springer-Verlag, New York, 2007.

[45] Krauskopf, B., Osinga, H. M., Doedel, E. J., Henderson, M. E., Guckenheimer, J., Vladimirsky, A., Dellnitz, M., Junge, O., A survey of methods for computing (un)stable manifolds of vector fields, *Internat. J. Bifur. Chaos Appl. Sci. Engrg.* **15**(3) (2005), 763–791.

[46] Kuznetsov, Yu. A., *Elements of Applied Bifurcation Theory.* Springer-Verlag, New York, 2^{nd} edition, 1998.

[47] Langfield, P., Krauskopf, B., Osinga, H. M., Solving Winfree's puzzle: the isochrons in the FitzHugh-Nagumo model, *Chaos* **24**(1) (2014), 013131.

[48] Lorenz, E. N., Deterministic nonperiodic flows, *J. Atmosph. Sci.* **20** (1963), 130–141.

[49] Mauroy, A., and Mezić, I., On the use of Fourier averages to compute the global isochrons of (quasi) periodic dynamics, *Chaos* **22**(3) (2012), 033112.

[50] Mauroy, A., Mezić, I., and Moehlis, J., Isostables, isochrons, and Koopman spectrum for the action-angle representation of stable fixed point dynamics, *Physica D* **261** (2013), 19–30.

[51] Mischaikow, K., Mrozek, M., Chaos in the Lorenz equations: A computer assisted proof, *Bull. Amer. Math. Soc.* **32**(1) (1995), 66–72.

[52] Mischaikow, K., Mrozek, M., Chaos in the Lorenz equations: A computer assisted proof part II: Details, *Math. Comput.* **67**(223) (1998), 1023–1046.

[53] Mischaikow, K., Mrozek, M., Szymczak, A., Chaos in the Lorenz equations: A computer assisted proof part III: Classical parameter values, *J. Diff. Equations* **169** (2001), 17–56.

[54] Nagumo, J. S., Arimoto, S., Yoshizawa, S., An active pulse transmission line simulating nerve axon, *Proc. Inst. Radio Engineers* **50** (1962), 2061–2070.

[55] Nowacki, J., Osinga, H. M., Brown, J. T., Randall, A. D., Tsaneva-Atanasova, K. T., A unified model of CA1/3 pyramidal cells: An investigation into excitability, *Progr. Biophys. Molec. Biol.* **105**(1-2) (2011), 34–48.

[56] Nowacki, J., Osinga, H. M., Tsaneva-Atanasova, K. T., Dynamical systems analysis of spike-adding mechanisms in transient bursts, *J. Math. Neurosci.* **2** (2012), 7.

[57] Nowacki, J., Osinga, H. M., Tsaneva-Atanasova, K. T., Continuation-based numerical detection of after-depolarisation and spike-adding threshold, *Neural Computation* **25**(4) (2013), 877–900.

[58] Osinga, H. M., Computing failure boundaries by continuation of a two-point boundary value problem, in *Proc. Ninth International Conference on Structural Dynamics*, Porto, Portugal (in press).

[59] Osinga, H. M., Krauskopf, B., Hittmeyer, S., Chaos and wild chaos in Lorenz-type systems, in Al-Sharawi, Z., Cushing, J., Elaydi, S. (eds.) *19th International Conference on Difference Equations and Applications.* Springer-Verlag, New York (in press).

[60] Osinga, H. M., Moehlis, J., Continuation-based computation of global isochrons, *SIAM J. Appl. Dynam. Syst.* **9**(4) (2010), 1201–1228.

[61] Osinga, H. M., Tsaneva-Atanasova, K. T., Geometric analysis of transient bursts, *Chaos* **23**(4) (2013), 046107.

[62] Palis, J., de Melo, W., *Geometric Theory of Dynamical Systems.* Springer-Verlag, New York, 1982.

[63] Palis, J., Takens, F., *Hyperbolicity & Sensitive Chaotic Dynamics at Homoclinic Bifurcations.* Cambridge University Press, Cambridge, 1993.

[64] Perelló, C., Intertwining invariant manifolds and Lorenz attractor, in *Global Theory of Dynamical Systems*, pp. 375–378. Proc. Internat. Conf., Northwestern Univ., Evanston, IL, Lecture Notes in Math. **819**, Springer-Verlag, Berlin, 1979.

[65] Rand, D., The topological classification of Lorenz attractors, *Math. Proc. Cambridge Philos. Soc.* **83** (1978), 451–460.

[66] Rinzel, J., Bursting oscillations in an excitable membrane model, in Sleeman, B. D., Jarvis, R. J. (eds.) *Ordinary and Partial Differential Equations (Dundee, 1984)*, pp. 304–316. Lecture Notes in Math. **1151**, Springer-Verlag, New York, 1985.

[67] Rinzel, J. A formal classification of bursting mechanisms in excitable systems, in Gleason, A. M. (ed.) *Proc. Int. Congress Math., Berkeley 1986* Vol. 1, 2, pp. 1578–1593. Amer. Math. Soc., Providence, RI, 1987; also (with slight differences) in Teramoto, E., Yamaguti, M. (eds.) *Mathematical Topics in Population Biology, Morphogenesis and Neuroscience*, pp. 267–281. Lecture Notes in Biomath. **71**, Springer-Verlag, Berlin, 1987.

[68] Robinson, C., *Dynamical Systems: Stability, Symbolic Dynamics, and Chaos.* CRC Press LLC, Boca Raton, FL, 2^{nd} edition, 1999.

[69] Sherwood, W. E., and Guckenheimer, J., Dissecting the phase response of a model bursting neuron, *SIAM J. Appl. Dynam. Syst.* **9**(3) (2010), 659–703.

[70] Sparrow, C., *The Lorenz Equations: Bifurcations, Chaos and Strange Attractors.* Appl. Math. Sci. No. **41**, Springer-Verlag, New York, 1982.

[71] Stern, J. V., Osinga, H. M., LeBeau, A., Sherman, A., Resetting behavior in a model of bursting in secretory pituitary cells: Distinguishing plateaus from pseudo-plateaus, *Bull. Math. Biol.* **70**(1) (2008), 68–88.

[72] Takeshita, D., Feres, R., Higher order approximation of isochrons, *Nonlinearity* **23**(6) (2010), 1303–1323.

[73] Tucker, W., The Lorenz attractor exists, *C. R. Acad. Sci. Paris Sér. I Math.* **328**(12) (1999), 1197–1202.

[74] Turaev, D. V., Shilnikov, L. P., An example of a wild strange attractor, *Mat. Sb.* **189** (1998), 291–314.

[75] Turaev, D. V., Shilnikov, L. P., Pseudo-hyperbolicity and the problem on periodic perturbations of Lorenz-like attractors, *Russian Dokl. Math.* **77** (2008), 17–21.

[76] Viana, M., What's new on Lorenz strange attractors? *Math. Intell.* **22**(3) (2000), 6–19.

[77] Williams, R. F., The structure of Lorenz attractors, *Publ. Math. IHES* **50** (1979), 101–152.

[78] Winfree, A. T., Patterns of phase compromise in biological cycles, *J. Math. Biol.* **1**(1) (1974), 73–93.

[79] Winfree, A. T., *The Geometry of Biological Time*. Interdisc. Appl. Math. **12**, 2^{nd} edition, Springer-Verlag, New York, 2001.

[80] Yorke, J. A., Yorke, E. D., Metastable chaos: The transition to sustained chaotic behavior in the Lorenz model, *J. Stat. Phys.* **21** (1979), 263–277.

[81] Zhang, W., Krauskopf, B., Kirk, V., How to find a codimension-one heteroclinic cycle between two periodic orbits, *Discr. Contin. Dynam. Syst. – Ser. A* **32**(8) (2012), 2825–2851.

Department of Mathematics
The University of Auckland
Private Bag 92019
Auckland 1142, New Zealand
E-mail: h.m.osinga@auckland.ac.nz